ANS RPSD 2018–20th Topical Meeting of the Radiation Protection & Shielding Division of ANS
Santa Fe, NM, August 26–31, 2018, on CD-ROM, American Nuclear Society, LaGrange Park, IL (2018)

SAND2018-7602C

ELECTRON TRANSPORT ALGORITHMS IN THE INTEGRATED TIGER SERIES (ITS) CODES

Brian C. Franke[1] and Ronald P. Kensek[1]

[1]*Sandia National Laboratories, Albuquerque, NM 87185, bcfrank@sandia.gov, rpkense@sandia.gov*

We describe the three electron-transport algorithms that have been implemented in the ITS Monte Carlo codes. While the underlying cross-section data is similar, each uses a fundamentally unique method, which at a high level are best characterized as condensed history, multigroup, and single scatter. Through a set of comparisons with experimental data and some comparisons of purely numerical results, we discuss various attributes of each of the algorithms and show some of the defects that can affect results.

I. INTRODUCTION

There are three fundamentally different electron-transport algorithms implemented in the Integrated TIGER Series (ITS) Monte Carlo codes[1]. The condensed-history method is still largely based on the algorithm adapted from the ETRAN code[2]. A hybrid multigroup/continuous-energy method[3] was implemented based on multigroup cross-section data, primarily to enable adjoint simulations. Recently, a single-scattering method was implemented based on the LLNL Evaluated Data Libraries (EDL)[4–6], with an analog capability and a cross-section moment-preserving method for acceleration[7]. All of the results presented here use only the analog capability of the single-scatter algorithm, and for the purposes of the remainder of this paper, the terms analog and single scatter can be thought of interchangably.

In Section II, we discuss each of the algorithms in detail, providing an overview of the data used by the algorithms and discussing various aspects of the algorithm implementations. In Section III, we use various test problems to motivate discussions about the methods, the data, and the implementations. In Section IV, we offer some conclusions and topics that warrant further investigation.

II. ELECTRON TRANSPORT ALGORITHMS

All three methods use similar data. We first present an overview of the similarities and differences. Then, in subsections on each method, we provide greater detail.

For elastic angular scattering, a high-energy factorization is used for a screened Mott representation while fits to the Riley distributions are used between 1-256 keV. For the condensed-history and hybrid multigroup/continuous-energy, the high-energy factorization is used above 256 keV using Seltzer's modified screening parameter to help the transition[8]. The single-scattering uses the factorization above 10 MeV with a logarithmic cubic spline to fill the gap for the total elastic cross section, but leaving the gap unfilled for the elastic differential in angle, relying instead on user-implemented interpolation of the data.

All three methods use the bremsstrahlung production and spectra cross sections of Seltzer[9,10]. The condensed-history uses angular distributions from Bethe-Heitler theory[11], while a simpler model is used for the multigroup/continuous-energy (similar to that used in MCNP[12]). None is provided in the EDL, and in this paper we explore the difference between using the direction of the electron with using a simple angular distribution.

The relaxation cascades are similar for the multigroup and condensed history, though there are minor differences. Some details can be lost through the multigroup treatment unless groups are devoted to the line radiation. The single-scatter method uses a complete set of subshell data for relaxation.

Each of the three has a different energy-loss model, and differ in the treatment of both large and small energy-loss interactions.

II.A. Condensed History

The condensed-history method is based on pre-computed energy-loss and angular-scattering distributions. (In the nomenclature of Ref. 13, this is a Class I condensed history algorithm.) The tracking of the electron is separated into "steps" and "substeps." At the start of the step, the collisional energy loss is sampled from a straggling distribution. Except when encountering a material boundary, the electron is moved a pre-determined substep distance, which depends on the energy of the electron at the start of the step and the resident material. For each substep, the electron is moved straight-ahead and an angular scatter is applied at the end of the substep. Secondary production of knock-on electrons, bremsstrahlung photons, and relaxation radiation is applied after the completion of each substep at randomly assigned locations along the substep. The number of each of these secondaries is sampled based on the mean number expected based on the production cross section and distance traveled. For bremsstrahlung production, the number is sampled from a Poisson distribution. For knock-on electrons and electro-ionization relaxation events, integer numbers of events about the mean are sampled in proportions that preserve the mean.

Angular scattering is computed over a substep centered in the middle of a step using the Goudsmit-Saunderson infinite-medium expansion[14]. Angular deflections due to inelastic-scattering interactions are accounted for approximately by adjusting the elastic-scattering distribution using a $(Z+1)/Z$ correction[8].

Energy loss is sampled over a step from the Blunck-Leisegang distribution with a correction by Seltzer[8]. More recently a per-substep energy-loss straggling formulation has also been implemented, patterned on the implementation of Hughes[15], which has been shown to preserve the accuracy of the energy-loss distribution even with numerous material-boundary crossings. This energy-loss sampling accounts for inelastic and excitation events and does not account for energy loss due to bremsstrahlung production, which is modeled separately.

The Jordan-Mack algorithm is used for boundary crossings[16]. An electron substep that intersects a material boundary is truncated at the boundary. An alternative angular-deflection distribution is applied that combines a Gaussian approximation for small angular deflections and samples an appropriate number of large angular deflections from the screened Rutherford distribution. This angular deflection is applied at the end of the substep, which coincides with the material boundary. Recently a code option was implemented to permit electrons to backscatter at these boundaries and has been shown to increase the accuracy of simulations in selected test problems.

Bremsstrahlung photon production, knock-on electron production, and electro-ionization events are sampled over each substep. The energy of the sampled bremsstrahlung photons is deducted from the electron. That is, bremsstrahlung photons are sampled at all energies, including below the photon cutoff energy, and the energy of each sampled photon is deducted from the electron. A biasing option exists to artificially increase the bremsstrahlung production by scaling the cross section, but the natural production is still sampled to determined the energy loss of the electron. Knock-on electrons (above the cutoff energy) due to electro-ionization inelastic scattering are sampled from the Møller distribution and are not correlated to energy loss of the primary electron. Likewise, electro-ionization events are sampled that produce relaxation radiation but are not correlated to the primary electron energy loss or to the production of knock-on electrons. Two models exist for sampling the relaxation radiation. The "standard codes" option only accounts for ionization of the K-shell for the highest atomic-number element in each material. The "PCODES" option has a more detailed model of the relaxation cascade, which, for every element, accounts for the K-shell, L-shells, an average binding-energy M-shell, and an average binding-energy N-shell. All condensed-history results reported in this article use the PCODES option.

When an electron reaches the cutoff energy, it is "kicked" if the electron range is such that it could reach a zone boundary (possibly a material boundary) or a subzone boundary (a tally region boundary). The kicking algorithm moves the electron in its direction of flight by a random fraction of its remaining practical range. This can have some effect on the energy-deposition and charge-deposition distributions and result in the tally of escaping electrons below the cutoff energy.

II.B. Hybrid Multigroup/Continuous-Energy

The multigroup-based transport uses cross-section data calculated by the CEPXS code[17]. The physics models in CEPXS were largely based on those that had been implemented in ITS and are, therefore, very similar. The CEPXS code integrates the cross section over each energy group or in the case of energy-loss cross sections integrates over both the energy group scattered from and the energy group scattered to. The multigroup integrations are based on a "flat" flux weighting, which is equivalent to the absence of a weighting function and simply integrating over the cross sections. CEPXS also integrates angular scattering moments for each cross section.

The angular moments and group-to-group cross sections are summed across all interaction types. This has a number of important implications for the implementation in ITS. The multigroup ITS code does not distinguish between the types of physical interactions. The method does not preserve correlations within sampled events, only statistical averages. For example, while tracking an electron one cannot distinguish between an energy-loss event due to bremsstrahlung production and due to an inelastic collision. A high-energy electron interaction may result in a lower energy electron and a high-energy photon, such that it resembles bremsstrahlung production, but the energies of the electron and photon may not sum to the energy of the incident electron. Such an event could also result in only a high-energy photon such that it does not resemble any actual physical process. The sampled events and tracking of the particles will accurately converge to the expected value of the particle flux and can be used to accurately calculate derived quantities such as energy and charge deposition, particle escape, etc. The method cannot be used to calculate quantities similar to a pulse-height distribution that depend on correlations between particles within a history.

CEPXS calculates angular scattering moments, which are converted to discrete scattering angles by a generalized Gauss-quadrature approach[18], which preserves the total interaction cross section and a selected number of angular scattering moments. (By default, 15 angular scattering moments are preserved.) This is applied to all group-to-group and within-group scattering, and thus for electrons applies to inelastic scattering, elastic scattering, and bremsstrahlung photon production. The discrete scattering angles can lead to artifacts in the simulation results. A separate precise-sampling treatment is allowed for interactions for which the model is an isotropic angular distribution of particles, such as in the production of Auger electrons, fluorescence photons, or annihilation photons.

There are two unique treatments in the case of electron elastic scattering. A Fokker-Planck approximation is ap-

plied, and the total elastic interaction cross section is deliberately not preserved within the simulation.

The moments for the Fokker-Planck term are deducted based on the difference in the two highest electron elastic angular-scattering moments. This is approximated in the Monte Carlo simulation by a single discrete scattering angle that preserves the transport moment (that is, preserving the difference between the total cross section and the first angular moment of the cross section). The cross section for this discrete-angle scatter is determined by the transport moment and the selected scattering angle. The angle should be very forward, as the Fokker-Planck model is only achieved in the limit that the cosine of the scattering angle approaches 1, but in that limit the cross section approaches infinite, so a compromise must be made. By default, ITS uses a scattering cosine of 0.95, but permits the user to select other values.

A Gauss-Radau quadrature is used for the electron elastic scattering, which includes the scattering cosine of $\mu_0 = 1$ corresponding to no angular deflection. Since elastic scattering interactions with no angular deflection are equivalent to a non-event, the cross section for these events is deducted from both the angular scattering distribution and from the total interaction cross section. This lack of preservation of the total interaction cross section, as simulated, serves to accelerate the simulation of the electron transport. In very thin problems, it can lead to underestimating the scattering of electrons and artifacts corresponding to uncollided electrons in the simulation.

The Møller distribution is used for large inelastic energy losses and knock-on production above the cutoff energy. A restricted stopping power accounts for soft energy losses, calculated as the difference between the ICRU stopping power and the large energy losses accounted for in group-to-group scattering. For fine energy-group structures, the group-to-group scattering due to the Møller distribution is limited to not exceed the ICRU stopping power. The restricted stopping power is treated as piece-wise constant in each group, and the continuous-slowing-down approximation (CSDA) is used. Distance to interaction is sampled for electrons (with reduced cross sections as described above) in the same manner as for photons. In electron tracking, the CSDA distance to a group boundary is compared against the distance to interaction and the distance to geometry boundary to determine which of these particle events occurs next.

Bremsstrahlung cross sections are evaluated for the photon production, photon angular distribution, and corresponding electron energy loss. Cross sections are also evaluated for the impact ionization that produces relaxation radiation in the form of fluorescence photons and Auger electrons.

The multigroup cross-section matrix is inverted to effect adjoint transport. Aside from a special treatment of the stopping power[19], the transport algorithm and cross section models are generally as described above for the multigroup code. There are certainly other important considerations in the adjoint method, but as the adjoint capability is not used in this paper, we refer the interested reader to previous publications[3].

II.C. Single Scattering

The single-scattering transport is based on the LLNL EDL. The EDL cross-section data is represented in tabulated forms with mostly prescribed interpolation schemes. Two notable features of the EDL are extension of cross section data below 1 keV and inclusion of the full set of ionization and relaxation data.

Four types of cross sections are included in the Evaluated Electron Data Library (EEDL): ionization, elastic scatter, bremsstrahlung, and excitation. In all cases, data is tabulated as a function of the incident electron energy, with different energy grids used for each set of data. For each interaction type, the total interaction cross section is included. The ionization data includes the cross section for ionization of each subshell and the electron energy-loss distribution for each subshell[9]. The elastic-scattering data includes angular distributions: isotropic at 10 eV, based on fits to the Riley data from 1-256 keV, and based on a high-energy factorization for a screened Mott representation at selected energies of 10 MeV and above. The bremsstrahlung data includes the photon energy spectra and an average electron energy-loss per bremsstrahlung interaction. The excitation data includes only the average energy loss per interaction.

In some cases, we have implemented models that supplement the data. For elastic scattering, it is prescribed that small angle scattering is to be modeled using the screened Rutherford distribution with Seltzer's screening parameter formula[8] and a cross section magnitude anchored to the elastic scattering cross section at $\mu_0 = 0.999999$. For electron ionization, we include angular deflections based on particle kinematics. For bremsstrahlung, we have implemented the photon angular distribution that is also used in CEPXS and the ITS "simple-brems" model. Contrary to the guidance with the data, we correlate the energy of the bremsstrahlung photon with the energy loss of the incident electron, as we expect this is a more accurate model than using the average electron energy loss.

The single-scatter algorithm for elastic and inelastic electron interactions makes electron transport much more computationally expensive, though it can be reasonably applied to low-energy problems. Options to accelerate the single-scatter algorithm are being developed. A moment-preserving discrete-angle method like that used for the multigroup code has been implemented for elastic scattering[7]. A similar method is under development for electro-ionization energy-loss cross sections.

We attempt to maintain all particle correlations in our implementation. For example, in an electro-ionization event,

the energy loss of the incident electron is the sum of the binding energy of the ionized shell and the secondary knock-on electron, and the ionized shell is relaxed consistent with the Evaluated Atomic Data Library (EADL).

III. RESULTS

In this section we compare numerical results using the three electron transport algorithms against experimental results from seven different experiments. In one final test problem, we compare only numerical results to highlight a specific feature. For distributional quantities, we use histograms to illustrate the bins over which Monte Carlo tallies were averaged. Where available, we have included error bars as an indication of uncertainty in the experimental results. Statistical uncertainty on the Monte Carlo results is not shown. We generally achieved a relative statistical uncertainty less than 2.5%. We deem this sufficient for having adequate confidence in the Monte Carlo convergence. It is also usually sufficient for establishing agreement or disagreement between results. Where the statistical uncertainty is higher, we attempt to describe the relevant statistical uncertainty levels.

III.A. Lockwood Albedo

In Fig. 1, we show the experimental results for the Lockwood electron charge-deposition data in uranium[20]. While the experiment measured charge deposition, the results were reported as the complement (that is, the albedo from the slab of material). In Figs. 2-4, we compare all three algorithms against the charge-deposition data. Analog results show issues above 256 keV. We attribute this to the sparse elastic angular-scattering data and the need to interpolate from the Riley distribution at 256 keV to the Mott distribution at 10 MeV. Otherwise, there is consistency in the trends of the comparison of the computational results to the experimental results. That could be only because all three are based on the same electron elastic-scattering data. The condensed-history results are consistently higher than the multigroup results. The multigroup results are consistently higher than the analog results. It is known that the condensed-history algorithm systematically underestimates electron reflection due to the straight-ahead substep mechanics.

III.B. Hanson Angular Scattering

In Fig. 5, we compare against the experimental measurements of Hanson[21] for the angular distribution of normally incident 15.7 MeV electrons transmitted through a gold foil with a thickness of 9.658 μm. The condensed-history results are in very good agreement with the experimental data. It is worth noting that the foil thickness is less than a substep, therefore all primary electrons are moved directly across the foil, and the boundary-crossing logic is used to evaluate the angular distribution. Therefore, for the condensed-history result, this is an evaluation of the angular deflection used

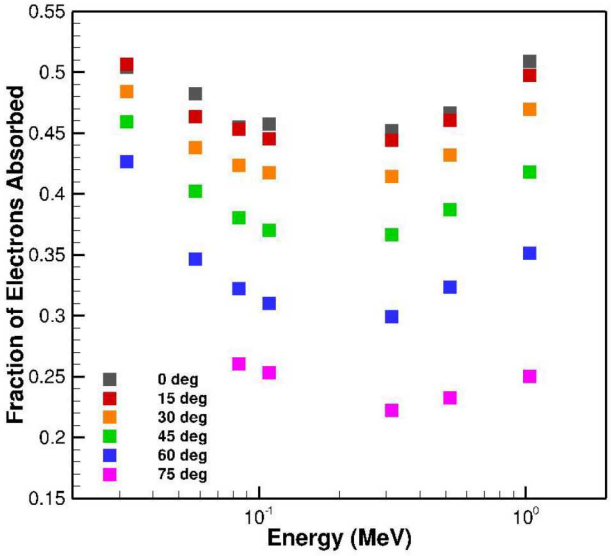

Fig. 1. Lockwood electron deposition experimental results.

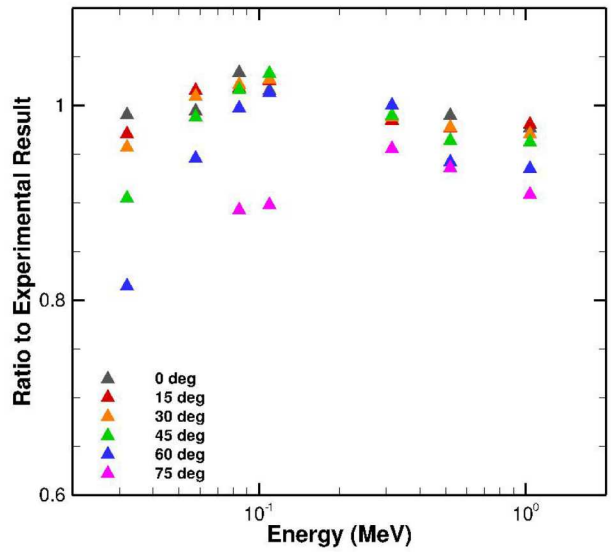

Fig. 2. Ratio of ITS condensed history to experiment.

in the Jordan-Mack algorithm rather than the Mott angular scattering distribution. The multigroup is also in good agreement, but required non-default settings in the cross-section generation to achieve this accuracy. The analog results underestimate the electron transmission at small angular deflections.

One would expect the analog electron-transport model to perform well in such a thin problem. However, we see significant differences compared with the experimental data

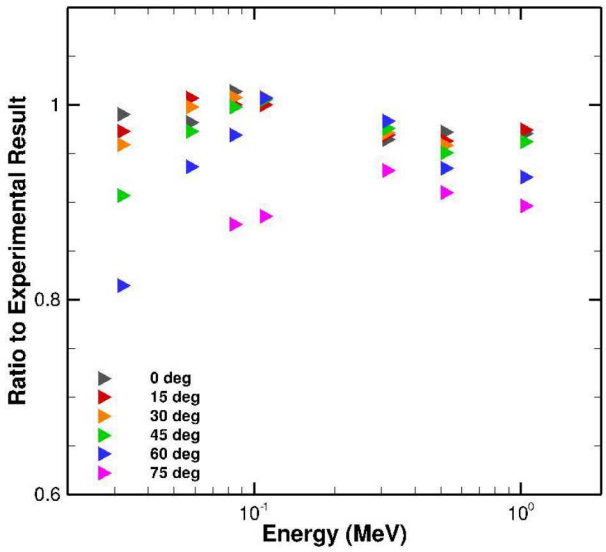

Fig. 3. Ratio of ITS multigroup to experiment.

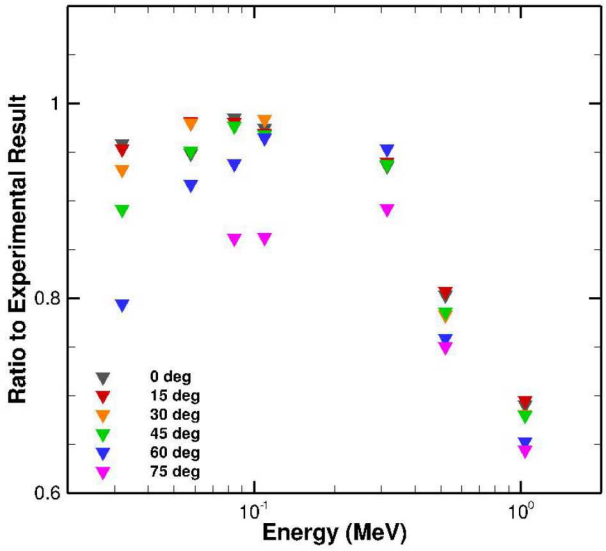

Fig. 4. Ratio of ITS analog to experiment.

and the condensed-history results. Fig. 6 shows additional numerical results for both the condensed-history and analog algorithms at 10 and 32.5 MeV, which coincide with the energy grid points at which elastic angular distributions are provided for gold in the EEDL. We observe good agreement at 32.5 MeV, but significant differences at 10 MeV. The combination of these results may indicate an inaccuracy in the angular distribution at 10 MeV, but further investigation is required.

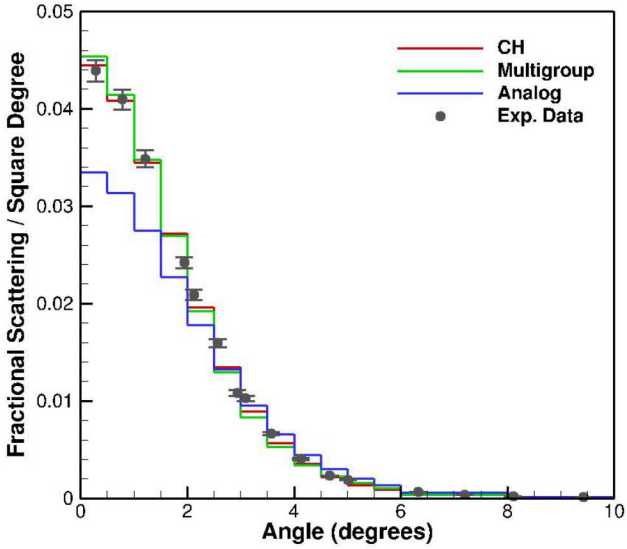

Fig. 5. Angular distribution of electrons transmitted through a gold foil.

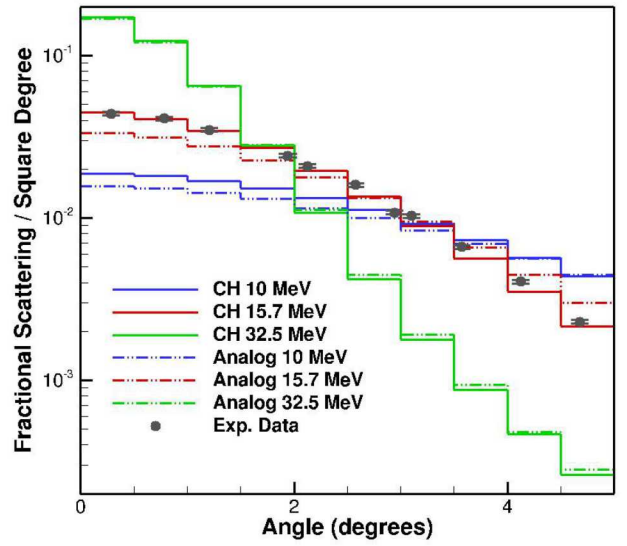

Fig. 6. Angular distribution of electrons transmitted through a gold foil at 10, 15.7, and 32.5 MeV.

Accurate multigroup results required two changes from the default settings for cross-section generation. In such a thin problem, it is necessary for the electrons to undergo a sufficient number of interactions in the simulation to avoid artifacts due to uncollided electrons and artifacts due to the discrete scattering angles. The multigroup results shown in Fig. 5 used a Fokker-Planck scattering an-

gle of $\mu_{FP} = 0.99999$ and used 63 angular scattering moments. The artifacts from the discrete-scattering model in the multigroup code are illustrated in Fig. 7, where the Fokker-Planck scattering angle was increased from the default value of $\mu_{FP} = 0.95$ to values of $\mu_{FP} = 0.999$ and $\mu_{FP} = 0.99999$. The relative statistical uncertainty for the relatively low transmission values with $\mu_{FP} = 0.95$ ranged up to 7.5%, but this was deemed adequate to observe the discrete scattering artifacts and the large errors relative to the other results.

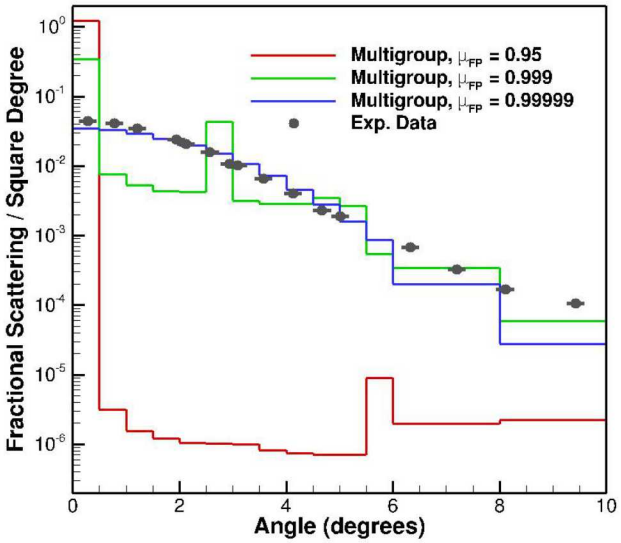

Fig. 7. Variation of the Fokker-Planck scattering angle in calculating the electron transmission through a gold foil.

The Fokker-Planck scattering model is of limited accuracy for the forward-peaked electron elastic scattering. The dominance of the Fokker-Planck angular approximation in this problem causes the distribution to become Gaussian in angle[22]. It is also necessary to increase the number of angular scattering moments that are preserved, which increases the number of discrete scattering angles. Fig. 8 shows the effect of increasing the number of angular scattering moments to 63 from the default of 15.

III.C. Tabata Charge Deposition

In Fig. 9, the computational results of all three electron-transport methods are compared against the charge-deposition data of Tabata for 14.9 MeV electrons normally incident on beryllium[23]. The relative statistical uncertainty varies widely and is much higher than 2.5% in regions where the net electron deposition is near zero, but an indication of the generally good statistical estimates from the Monte Carlo calculations is that the one-sigma standard deviation for each of the deposition values is less than

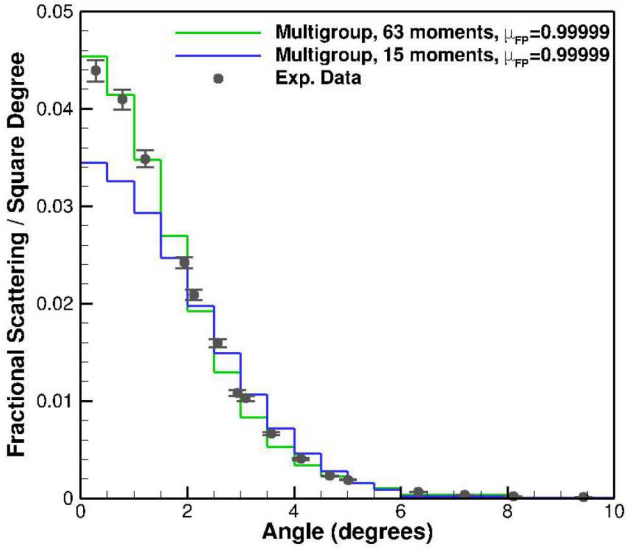

Fig. 8. Effect of the number of angular scattering moments in calculating the electron transmission through a gold foil.

0.005 electrons-cm^2/g, with the largest uncertainties near the peaks in the deposition distributions. The condensed-history and multigroup results give reasonable agreement with the data. Again, the analog simulation appears to be somewhat inaccurate. For beryllium, the elastic angular-scattering distribution data are provided at 10 and 21.25 MeV.

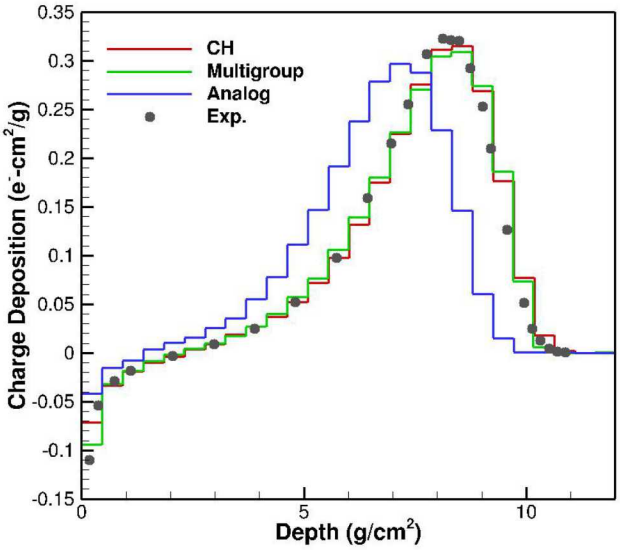

Fig. 9. Charge deposition as a function of depth in beryllium.

III.D. McLaughlin Energy Deposition in Aluminum

Fig. 10 compares the energy deposition of 3 MeV electrons normally incident on a slab of aluminum[24]. The statistical uncertainty in the Monte Carlo calculations is less than 2.5% up to a depth of 1.1 g/cm^2 in the analog results and up to a depth of 1.75 g/cm^2 in the condensed history and multigroup results. The condensed-history and multigroup calculations are in good agreement with the experimental data. The disagreement of the analog simulations may be due to the interpolation of the electron elastic-scattering distribution over a broad energy range, with the highest-energy data from the Riley distribution at 256 keV and the lowest-energy distribution from the Mott distribution at 10 MeV. Further investigation of the interpolation of these distributions is warranted.

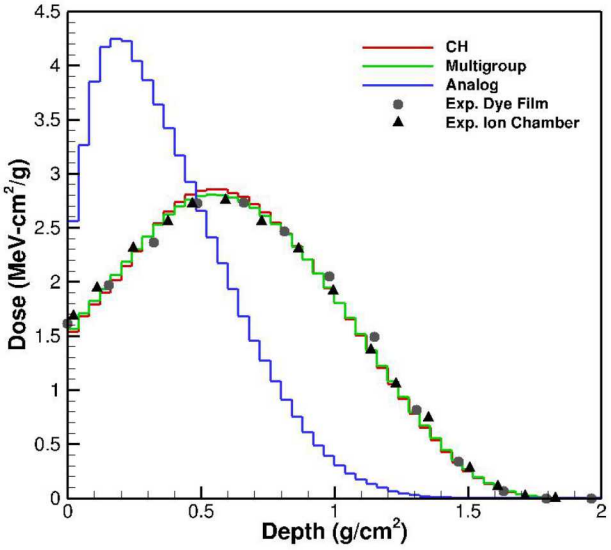

Fig. 10. Energy deposition versus depth in aluminum.

III.E. Sanford Bremsstrahlung Converter

We next examine a bremsstrahlung converter experiment that was composed of carbon and had an incident electron beam at 750 keV[25]. The geometry consists of a carbon cylinder with radius of 1 cm and thickness of 0.48 cm and a set of dose detectors 30 cm away in the direction of the beam and at varying radii. The thickness of the carbon is greater than the range of the incident electrons, and therefore the source electrons are not transmitted. The bremsstrahlung photons created by the electrons are transmitted through the carbon, and thus the carbon is said to "convert" the electron beam to bremsstrahlung photons. Fig. 11 compares calculated results with data for this experiment. Both the condensed-history and multigroup models show good agreement with the experimental data. The multigroup results were generated using 63 angular scattering moments and still show some effects of the discrete scattering angles in the production of the bremsstrahlung photons. Fig. 12 compares the multigroup results against results generated using the default of 15 angular scattering moments and shows much greater effects of the discrete scattering angles.

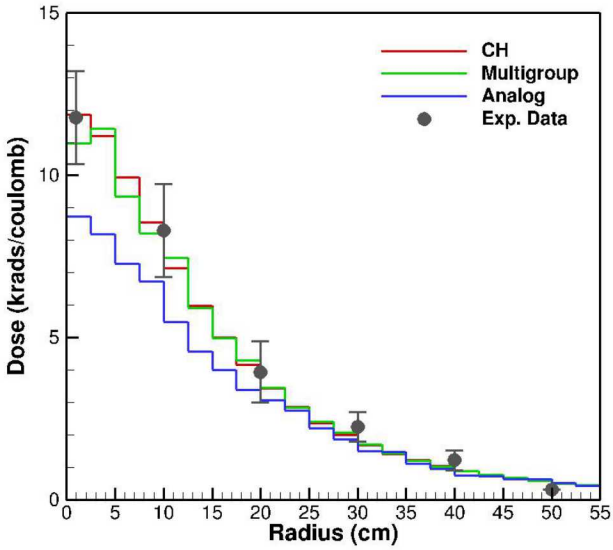

Fig. 11. Radial energy deposition due to bremsstrahlung photons produced by an electron beam stopped in carbon.

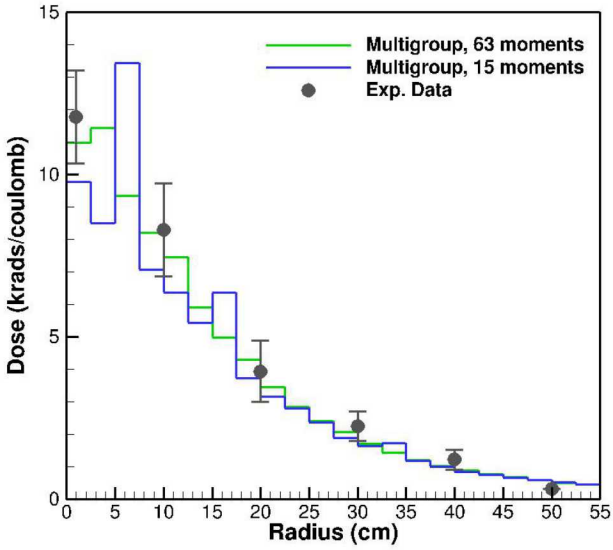

Fig. 12. Artifacts of discrete-angle scattering in bremsstrahlung production in multigroup simulations.

With a "simple brems" model, the analog simulation underestimates energy deposition at small radius, corresponding to forward-directed bremsstrahlung photons. The production of the photons is also dependent upon the initial electron transport in the converter, and it is possible that the underestimation observed in Fig. 11 is due to issues in the electron elastic-angular scattering model, similar to those previously observed in the Lockwood and McLaughlin comparisons. Fig. 13 shows that the analog results severely overestimate the forward-directed bremsstrahlung production when the bremsstrahlung photons are simply given the same direction of flight as the electron producing them (labeled "No Brems Angle" in the figure). A bremsstrahlung angular model is clearly required to accurately simulate this experiment. Without Monte Carlo biasing, which is mostly not yet implemented for the analog capability, this calculation is more computationally expensive. Higher statistical uncertainties were considered adequate to observe the differences with the experiment and other numerical results. The statistical uncertainty on the "Simple Brems" results (labeled simply as "Analog" in Fig. 11) range between 3.5% and 11.5%. The statistical uncertainty on the "No Brems Angle" results range between 11.5% and 26.5%.

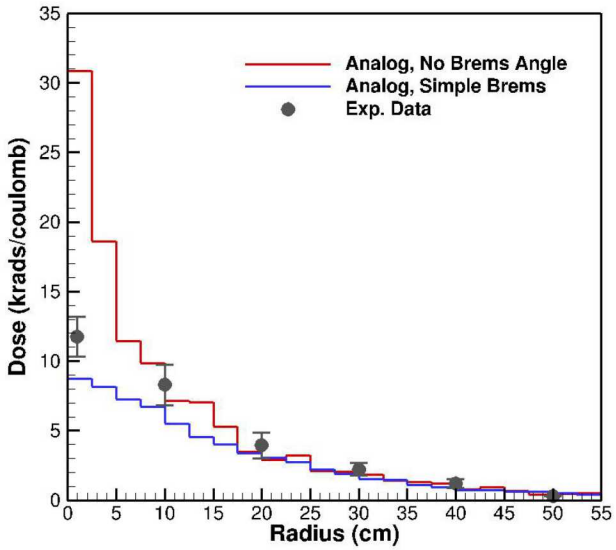

Fig. 13. Two models for the angular distribution of the production of bremsstrahlung photons in the analog simulation.

III.F. McLaughlin Energy Deposition in Polystyrene

Fig. 14 compares numerical results against experimental data[24] for a 100 keV electron beam normally incident on polystyrene. The statistical uncertainty on the Monte Carlo results was less than 2.5% up to a depth of 15 mg/cm^2. Here we see good agreement among all of the methods and the data. There is disagreement with the experimental results in the tails of the distribution at a depth of about 15 mg/cm^2, but all of the calculations are in close agreement there at the practical range of the electrons.

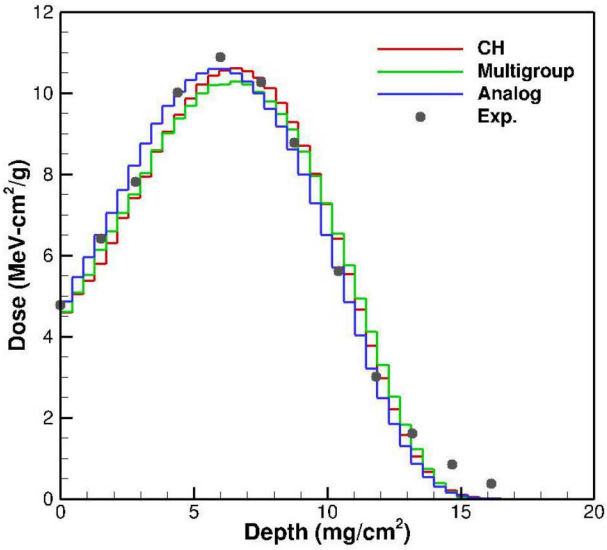

Fig. 14. Energy deposition versus depth in polystyrene.

III.G. Dolan Photoemission

Comparison with the Dolan experimental data for reverse photoemission from tantalum[26] is shown in Fig. 15. In this experiment a bremsstrahlung spectrum of source photons was incident on a slab of tantalum and the energy spectrum of electron emission was measured from the incident surface. All of the numerical results below 33 keV have a relative statistical uncertainty less than 1.5%. The calculations are in good agreement with each other above 10 keV, but differ from the experimental results below about 20 keV. Below 10 keV, there are a large number of Auger and fluorescence energies from the L-shells of tantalum, so differences in the relaxation data likely account for the differences in the calculations.

III.H. 4 keV Photoemission

All of the results presented so far show our implementation of the analog capability to be either less accurate or no better than the condensed-history capability. While we do not yet have a comparison with validation data showing the benefits of the analog capability, it is worthwhile to show a code comparison that illuminates a significant difference and anticipated benefit. Fig. 16 compares reverse photoemission from gold for a 4-keV photon source. These results are very sensitive to properly accounting for the binding en-

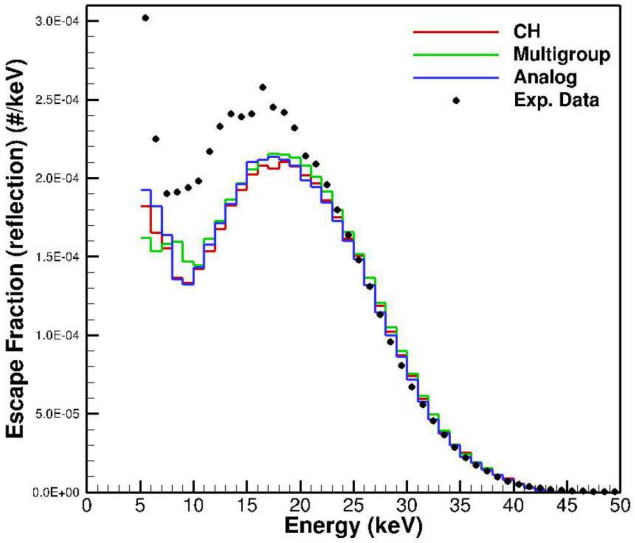

Fig. 15. Reflected electron photo-emission from a tantalum slab.

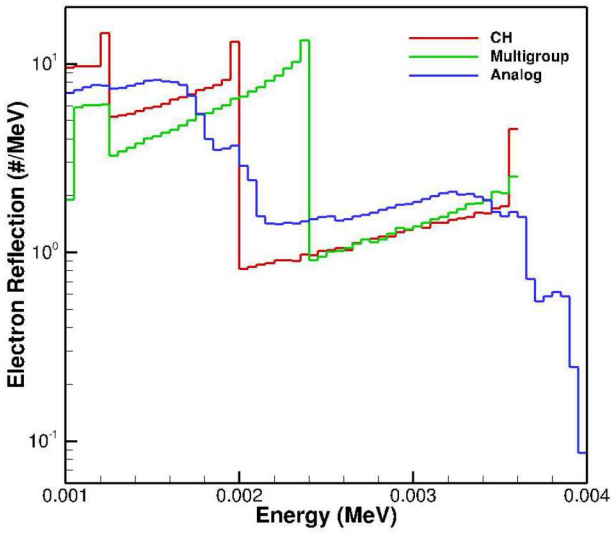

Fig. 16. Reflected electron photo-emission from a gold slab for 4 keV photons.

ergies in the photo-ionization and capturing the details of the relaxation cascade. Without comparison to experimental data, we cannot confirm the accuracy of the spectrum of photoelectrons and Auger electrons in these spectra, but we can see the stark difference that results from using the complete set of subshell data that is present in the EADL as compared to the more limited data in the condensed-history and multigroup codes, which use only average M-shell energies, "<M>", and average N-shell energies, "<N>", and neglect higher shells. The difference in the peaks at 2 and 2.4 keV between the condensed-history and multigroup results, respectively, shows that the average N-shell energy is sometimes being treated as zero, in this case only once in the <M>-2<N> Auger relaxation energy.

IV. CONCLUSIONS

We have provided a description of the electron-transport algorithms in the Integrated TIGER Series (ITS) codes. Comparisons have been made between the computational results of these algorithms and a variety of experimental data.

In general, we observe good agreement between the condensed-history results and the experimental data. The multigroup algorithm can also provide good agreement with the experimental data, though it sometimes required using cross-section generation parameters different from the default settings. In those cases, we also showed the results that were obtained using the default cross sections.

The analog algorithm did not provide good agreement in experiments with electron sources above 256 keV. Based on the investigations presented here, we have attributed this to the elastic angular scattering distributions, but further investigation is needed to better understand these issues and to rule out the possibility of defects in the implementation. For electron sources below 256 keV (and for the Dolan experiment starting with a source spectrum of bremsstrahlung photons up to 50 keV) we found good agreement between the analog results and experimental results.

Through a comparison of numerical results with a low-energy source, we offered a preliminary demonstration of one of the significant improvements offered by the analog capability. By utilizing a complete set of subshell data the analog simulation provides more detailed relaxation radiation. Future investigations will aim to demonstrate the improved accuracy provided by this more detailed model.

ACKNOWLEDGMENTS

Sandia National Laboratories is a multimission laboratory managed and operated by National Technology and Engineering Solutions of Sandia, LLC., a wholly owned subsidiary of Honeywell International, Inc., for the U.S. Department of Energy's National Nuclear Security Administration under contract DE-NA-0003525.

This paper describes objective technical results and analysis. Any subjective views or opinions that might be expressed in the paper do not necessarily represent the views of the U.S. Department of Energy or the United States Government.

REFERENCES

1. B. C. FRANKE, R. P. KENSEK, T. W. LAUB, and M. J. CRAWFORD, "ITS Version 6: The Integrated TIGER Series of Coupled Electron/Photon Monte Carlo Transport Codes, Revision 5," Tech. Rep. SAND2008-3331, Sandia National Laboratories (2013).

2. S. M. SELTZER, "An overview of ETRAN Monte Carlo methods," in T. M. JENKINS, W. R. NELSON, and A. RINDI, editors, "Monte Carlo transport of electrons and photons," Plenum Press, New York, Ettore Majorana international science series: Physical sciences (1988).

3. J. E. MOREL, L. J. LORENCE, R. P. KENSEK, J. A. HALBLEIB, and D. P. SLOAN, "A Hybrid Multigroup/Continuous-Energy Monte Carlo Method for Solving the Boltzmann-Fokker-Planck Equation," *Nucl. Sci. Eng.*, **124**, 369–389 (1996).

4. S. PERKINS, D. CULLEN, and S. SELTZER, "Tables and Graphs of Electron-Interaction Cross Sections from 10 eV to 100 GeV Derived from the LLNL Evaluated Electron Data Library (EEDL), Z=1,100," Tech. Rep. UCRL-50400 Vol 31, LLNL (1991).

5. D. CULLEN, M. CHEN, J. HUBBELL, S. PERKINS, E. PLECHATY, J. RATHKOPF, and J. SCOFIELD, "Tables and Graphs of Photon-Interaction Cross Sections from 10 eV to 100 GeV Derived from the LLNL Evaluated Photon Data Library (EPDL)," Tech. Rep. UCRL-50400 Vol 6, LLNL (1989).

6. S. PERKINS, D. CULLEN, M. CHEN, J. HUBBELL, J. RATHKOPF, and J. SCOFIELD, "Tables and Graphs of Atomic Subshell and Relaxation Data Derived from the LLNL Evaluated Atomic Data Library (EADL), Z=1,100," Tech. Rep. UCRL-50400 Vol 30, LLNL (1991).

7. D. M. FLETCHER and B. C. FRANKE, "Generalised Boltzmann Fokker-Planck Elastic Scattering using the Evaluated Electron Data Library," in "Proc. M&C 2017," Jeju, Korea (April 16-20 2017), american Nuclear Society (2017) (CD-ROM).

8. S. SELTZER, "Electron-Photon Monte Carlo Calculations: The ETRAN Code," *Appl. Radiat. Isot.*, **42**, *10*, 917–941 (1991).

9. S. M. SELTZER, "Cross Sections for Bremsstrahlung Production and Electron-Impact Ionization," in T. M. JENKINS, W. R. NELSON, and A. RINDI, editors, "Monte Carlo transport of electrons and photons," Plenum Press, New York, Ettore Majorana international science series: Physical sciences (1988).

10. S. M. SELTZER and M. J. BERGER, "Bremsstrahlung spectra from electron interactions with screened atomic nuclei and orbital electrons," *Nucl. Instrum. Meth.*, **B12**, 95–134 (1985).

11. H. W. KOCH and J. W. MOTZ, "Bremsstrahlung Cross-Section Formulas and Related Data," *Rev. Mod. Phys.*, **31**, *4*, 920–956 (1959).

12. H. G. HUGHES, "Recent developments in low-energy electron photon transport for MCNP6," *Progress in Nuclear Science and Technology*, **4**, 454–458 (2014).

13. M. J. BERGER, "Monte Carlo Calculations of the Penetration and Diffusion of Fast Charged Particles," in B. ADLER, S. FERNBACH, and M. ROTENBERG, editors, "Methods in Computational Physics, Vol. 1," Academic Press, New York (1963).

14. M. J. BERGER and R. WANG, "Multiple-scattering angular deflections and energy-loss straggling," in T. M. JENKINS, W. R. NELSON, and A. RINDI, editors, "Monte Carlo transport of electrons and photons," Plenum Press, New York, Ettore Majorana international science series: Physical sciences (1988).

15. H. G. HUGHES, "Improved Logic for Sampling Landau Straggling in MCNP5," in "Proc. M&C 2005," Palais des Papes, Avignon, Franke (September 12-15 2005), american Nuclear Society (2005) (CD-ROM).

16. D. JENSEN, *Monte Carlo Calculation of Electron Multiple Scattering in Thin Foils*, Master's thesis, Naval Postgraduate School, Monterey, CA (1988).

17. L. J. LORENCE, JR., J. E. MOREL, and G. D. VALDEZ, "Physics guide to CEPXS: a multigroup coupled electron-photon cross-section generating code," Tech. Rep. SAND89-1685, Sandia National Laboratories (1989).

18. D. P. SLOAN, "A New Multigroup Monte Carlo Scattering Algorithm for Neutral and Charged-Particle Boltzmann and Fokker-Planck Calculations," Tech. Rep. SAND83-7094, Sandia National Laboratories (1983).

19. J. A. HALBLEIB and J. E. MOREL, "Adjoint Monte Carlo electron transport in the continuous slowing-down approximation," *J. Comp. Phys.*, **34**, 211 (1980).

20. G. J. LOCKWOOD, L. E. RUGGLES, G. H. MILLER, and J. A. HALBLEIB, "Electron energy and charge albedos calorimetric measurement vs Monte Carlo theory," Tech. Rep. SAND80-1968, Sandia National Laboratories (1981).

21. A. O. HANSON, L. H. LANZL, E. M. LYMAN, and M. B. SCOTT, "Measurement of Multiple Scattering of 15.7-MeV Electrons," *Physical Review*, **84**, *4* (1951).

22. C. BÖRGERS and E. W. LARSEN, "On the accuracy of the Fokker-Planck and Fermi pencil beam equations for charged particle transport," *Medical Physics*, **23**, *10*, 1749–1759 (1996).

23. T. TABATA, R. ITO, and S. OKABE, "Charge Distribution Produced by 4 to 24 MeV Elecrons in Elemental Materials," *Physical Review B*, **3**, *3* (1971).

24. W. L. MCLAUGHLIN and E. K. HUSSMAN, "The Measurement of Electron and Gamma-Ray Dose Distributions in Various Media," in "Large Radiation Sources for Industrial Processes," IAEA-SM-123/43.

25. J. A. HALBLEIB, T. W. L. SANFORD, and W. BEEZHOLD, "Experimental Verification of Bremsstrahlung Dosimetry Predictions for 0.75 MeV Electrons," Tech. Rep. SAND85-1517, Sandia National Laboratories (1986).

26. K. W. DOLAN, "X-ray-Induced Electron Emission from Metals," *J. Appl. Phys.*, **46**, *6*, 2456–2463 (1975).